Supplementary Information (SI) for Journal of Materials Chemistry A.

SUPPLEMENRARY INFORMATION

Detonation nanodiamonds with ultra-pure surfaces thanks to a combination of chlorine and fluorine gas treatment

Killian Henry[1,2], Mélanie Emo[1], Sébastien Diliberto[1], Sébastien Hupont[1], Julien Parmentier[3], Sylvette Brunet[4], Jean-Dominique Comparot[4], Marc Dubois[2], Brigitte Vigolo[1,*]

[1] Université de Lorraine, CNRS, IJL, F-54000 Nancy, France
[2] Université Clermont Auvergne, CNRS, ICCF UMR 6296, 24 av. Blaise Pascal, F-63178 Aubière, France
[3] Institut de Science des Matériaux de Mulhouse, IS2M UMR CNRS 7361, 15, rue Jean Starcky - BP 2488, 68057 Mulhouse cedex
[4] Institut de Chimie des Milieux et Matériaux de Poitiers - IC2MP 7285, UMR CNRS, 4 rue Michel Brunet, 86073 Poitiers Cedex 9, France
* Corresponding author e-mail: Brigitte.Vigolo@univ-lorraine.fr

Table of content

1 Optimization of the chlorine-based treatment

1.1 Optimization of the duration of the chlorine-based treatment

Figure S1 shows the thermograms under air of the raw and the DND samples treated with Cl_2 at 600 °C for 1 h (in red), 2 h (in blue) and 4 h (in green) at a Cl_2 flowrate of 5 mL/min. After being treated under Cl_2, the DND combustion temperature is upshifted with the treatment temperature (Figures S1a and S1b) and the absence of dehydration (insert Figure S1a) is as well observed after treatment whatever the used conditions. After only 1 h of treatment, the remaining inorganic impurities are significantly reduced (from 3.5 ± 0.8 % down to 2 ± 0.8 %) and longer treatment durations do not allow a clear gain in inorganic content reduction by considering that limit of detection of TGA is reached (Figure S1c). Moreover, a darkening of the DND powder was observed after being heated at 600 °C for 2 and 4 h under Cl_2 atmosphere, probably causing a graphitization of the material, not desired here.

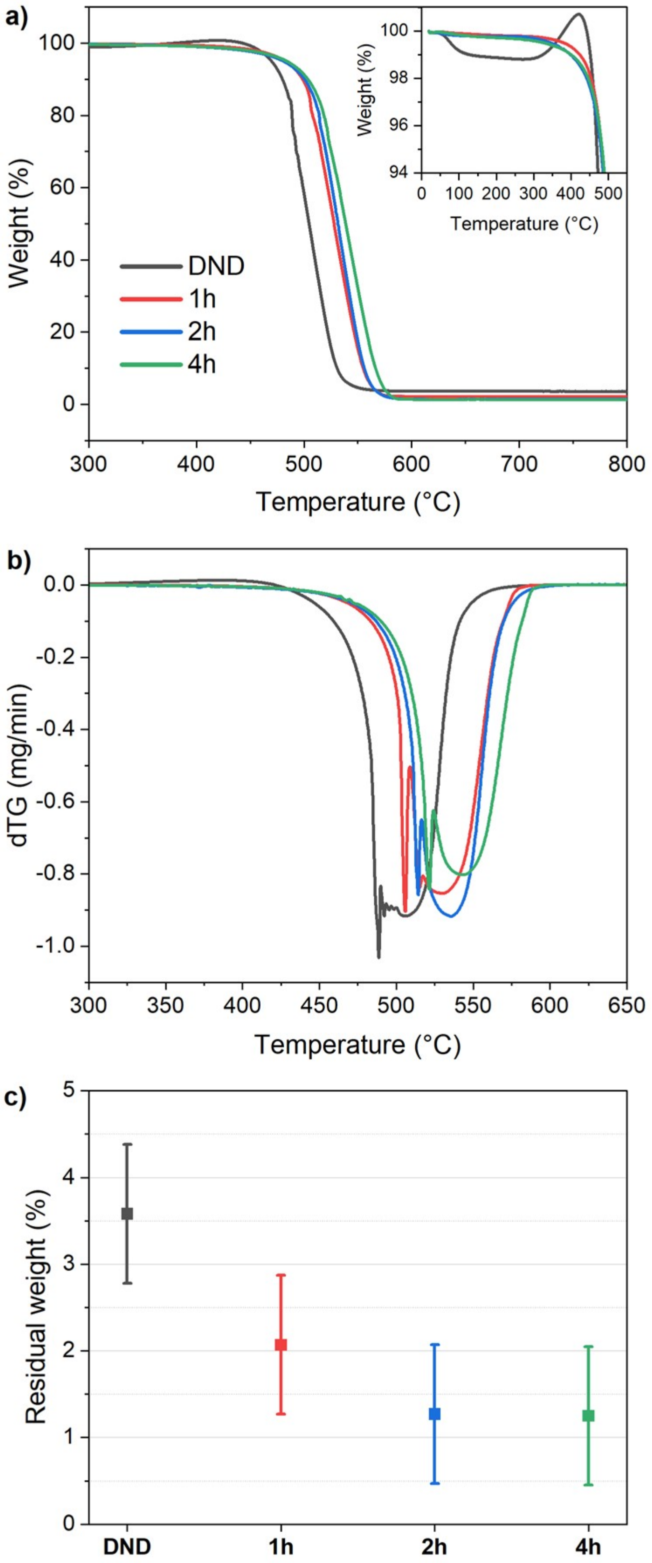

Figure S1 (a) Thermograms in air of the used DND powder treated under Cl_2 at 600 °C for 1, 2 and 4 h at a Cl_2 flowrate of 5 mL/min. The insert is a zoom in of low weight loss domain; (b) dTG representation of the thermograms of (a); (c) Remaining weights measured from the thermograms at 800 °C.

1.2 Optimization of the Cl_2 flowrate

Figure S2 exhibits the thermograms under air of DND powders treated during 1 h at 600 °C under chlorine with flowrates of 5, 7, 20 and 50 mL/min. An upshift in the DND combustion temperature (Figures S2a and S2b) and the absence of dehydration (insert Figure S2a) are observed regardless of the used Cl_2 flowrate. The remaining weight corresponding to the inorganic impurities after the DND combustion does not show any significant decrease when the Cl_2 flowrate is increased above 20 mL/min (Figure S2c). Moreover, it should be noted that a flowrate of 50 mL/min of Cl_2 is delicate to precisely control with the used apparatus.

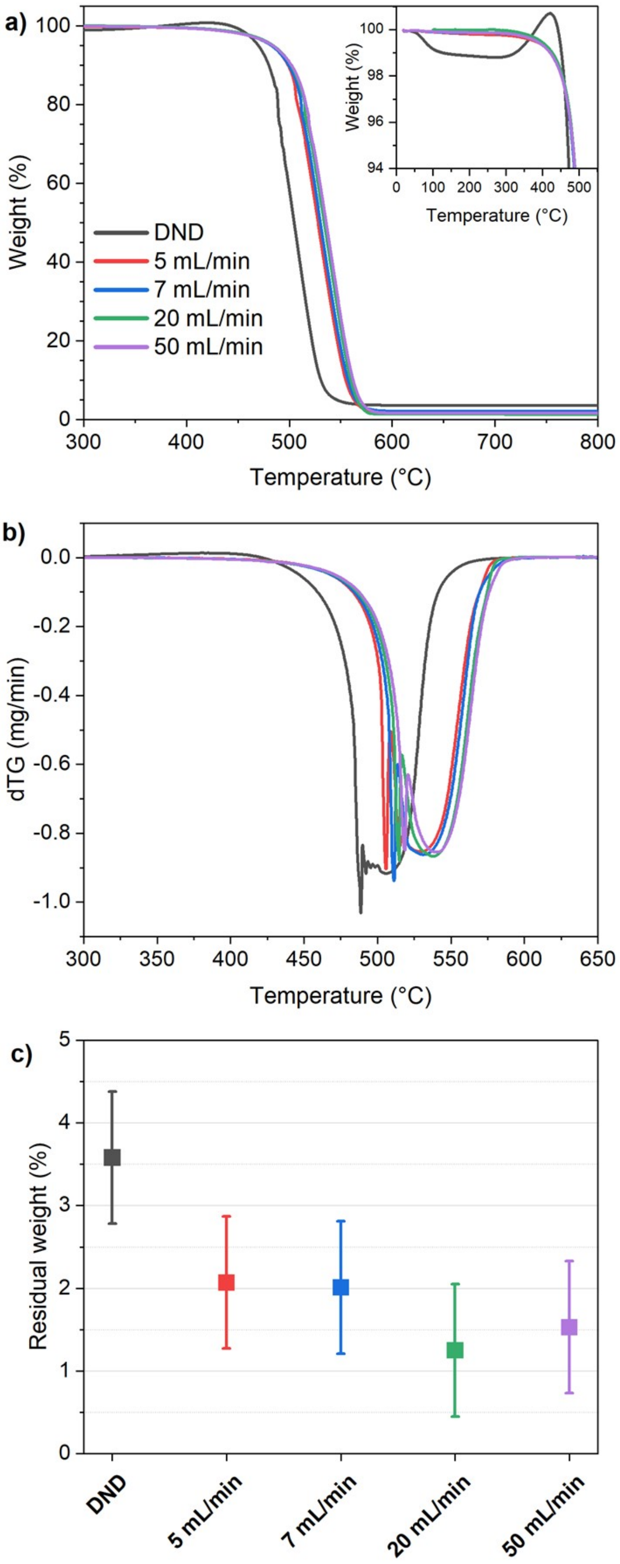

Figure S2 (a) Thermograms in air of the used DND powder treated under Cl_2 at during 1 h at 600 °C under Cl_2 with flowrates of 5, 7, 20 and 50 mL/min. The insert is a zoom in of low weight loss domain; (b) dTG representation of the thermograms of (a); (c) Remaining weights from the thermograms measured at 800 °C.

1.3 Modelization of the DND thermograms

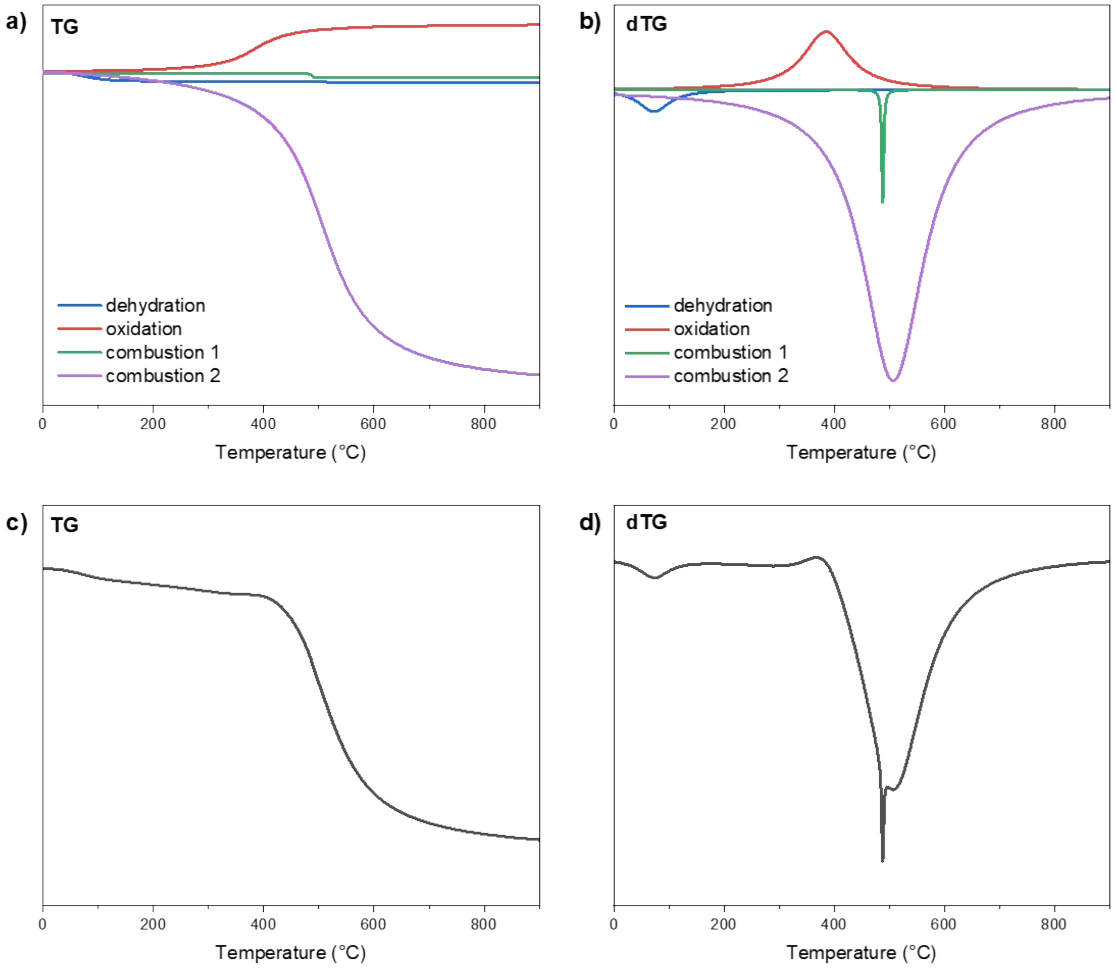

Figure S3 Modelization of the DND thermograms with the four behaviors possibly observable for DNDs heated under dry air: dehydration, metal oxidation, rapid (1) and slow (2) combustion: (a) sample weight evolution as a function of temperature, (b) its derivative with respect to time, (c) resulting weight loss evolution (sum of the 4 contributions shown in a), (d) resulting derivative curve with respect to time (sum of the 4 contributions shown in b).

2 Optimization of fluorine purification treatment

2.1 Exothermic reaction at ambient temperature

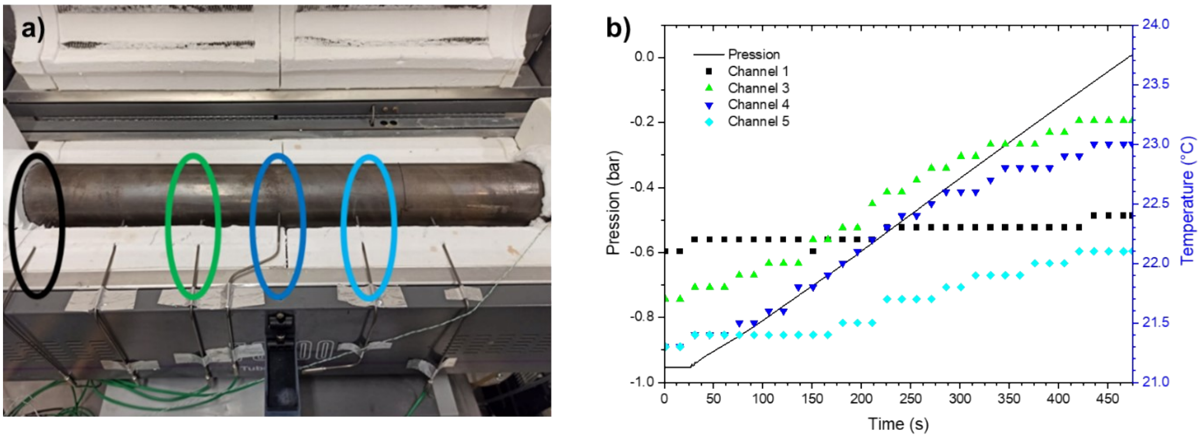

Figure S4 (**a**) Photograph of the 5 L-reactor used for DND fluorination, showing the location of the thermocouples in contact with the reactor to measure temperature (numbered 1 to 6, from left to right) and (**b**) changes over time in the temperatures measured by thermocouples 1, 3, 4 and 5 during fluorination and pressure increase of F_2.

Five thermocouples were placed at different locations along the nickel reactor. F_2 gas was injected on the left side of the reactor and 10 g of DNDs were loaded at positions 3, 4 and 5 inside the reactor. The temperature was observed to spontaneously increase due to the exothermicity of the fluorination started first on channels 3 and 4 and was slightly later on channel 5 (channel 1 is the control experiment, without DND). The front of the reaction was moved from position 3 and 4 to 5.

2.2 In-situ gas phase FTIR study

In-situ studies followed by gas phase FTIR spectroscopy were realized *i*) by increasing the temperature from RT up to 520 °C (in static condition) and *ii*) in static mode from 200 to 390 °C, then under dynamic flow of F_2 inside the opened reactor at 520 °C for 8 h are gathers in Figures S5 and S6, respectively.

Figure S5 displays the complete time-resolved spectra of the fluorination of the DND powder at RT. CF_4 vibration bands appear after a few minutes under F_2 atmosphere and are still present at 50 min of reaction at RT, that means the reaction is not complete under these conditions. However, release of HF, COF_2, CF_4 and SiF_4, molecules can be explained by the removal of C-H bonds, oxygenated groups, sp^2 carbon shells, and SiO_2 impurities, respectively.

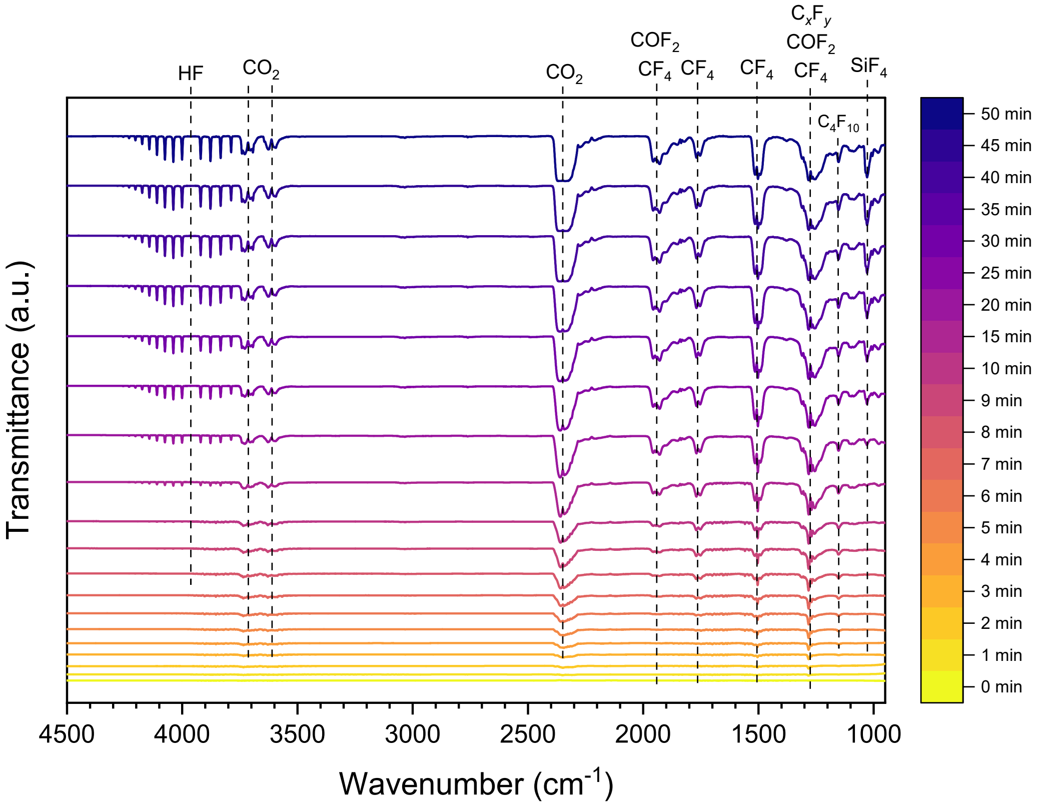

Figure S5 Gas phase FTIR spectra of DND during fluorination at room temperature.

After having investigating the fluorination mechanism involved at RT, temperature was further increased up to 520 °C. Rising the fluorination temperature from 200 to 520 °C in static conditions (Figure S6a) right after the first fluorination at RT allows the complete elimination of SiO_2 (absence of SiF_4 vibrations). The resulting FTIR spectra slowly become mainly composed by HF and CF_4 vibration bands. The same results are obtained for a fluorination under dynamic conditions and are shown in Figure S6b.

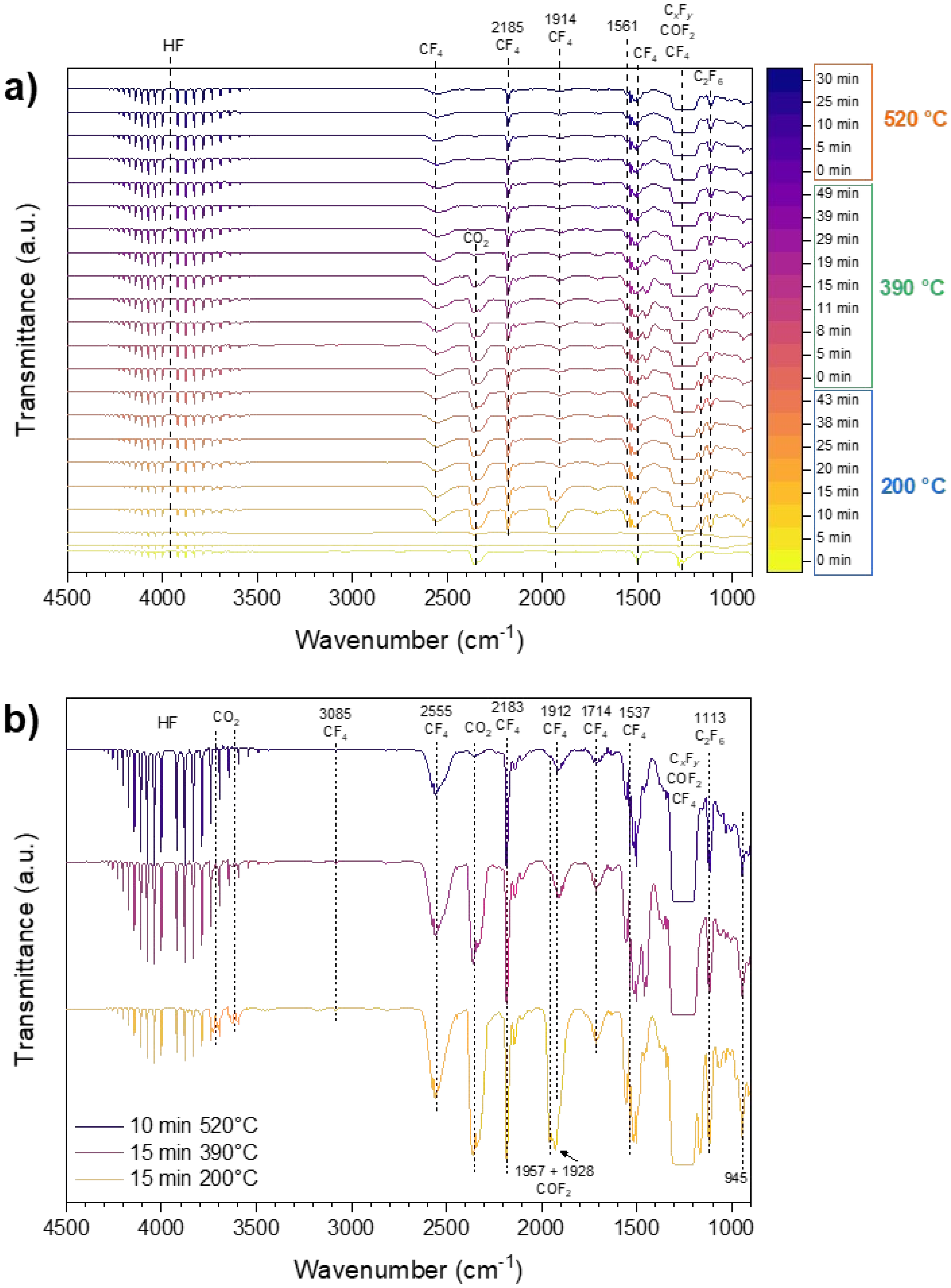

Figure S6 a) Gas phase FTIR spectra of DND during fluorination from 200 to 520 °C, in static condition. **b**) Selected spectra after 15 min at 200 °C (yellow) and 15 min at 390 °C (purple) under static condition and 10 min at 520 °C (blue) in dynamic condition.

Table S1 gathers the positions of the features expected for constituting the *R*- and *P*-branches of the rotational transitions of HF. The detected HF positions can be explained by selection rule. When the rotational quantum number $J \neq 0$, the transition between state ΔJ must be equal to 0, or ±1 ($\Delta J = 0, \pm 1$). Thus, when the transition $\Delta J = +1$ we obtain the so-called *R*-branch (*rich*) where the molecule gains rotational energy. Conversely, if $\Delta J = -1$ the molecule loses rotational energy and the *P*-branch (*poor*) is obtained. Also, if the transition between two states is equal to 0, then the *Q*-branch is obtained, characterizing the perpendicular vibrations, and located between the R and P branches [1–3].

Table S1 Observed positions of the rotational transitions of HF from FTIR.

R-branch	Wavenumber (cm^{-1})	*P*-branch	Wavenumber (cm^{-1})
R(0)	4000		
R(1)	4036	*P(1)*	3920
R(2)	4075	*P(2)*	3877
R(3)	4110	*P(3)*	3834
R(4)	4142	*P(4)*	3787
R(5)	4173	*P(5)*	3740
R(6)	4203	*P(6)*	3693
R(7)	4230	*P(7)*	3643
R(8)	4256	*P(8)*	3595
R(9)	4279	*P(9)*	3542

2.3 Investigation of paramagnetic defects of DNDs by EPR, a literature review

In the literature, the high spin density of DNDs (up to 10^{20} spin/g) is explained by several types of paramagnetic centers (PCs) [4–13] : *i*) transition metal impurities with a peak-to-peak linewidth, ΔH_{PP}, of several hundred Gauss and a g-factor close to 2.5; *ii*) structural defects (dangling bonds or DBs) with g = 2.003 and ΔH_{PP} in the range 4-11 G; *iii*) P_1 or N_0 centers corresponding to the substitution of carbon atoms by nitrogen ones with a similar value of g-factor than for DBs but a broader line. The typical narrow singlet quasi-Lorentzian-like line of DND can be then fitted with two Lorentzian lines with very close g-factor values, assigned to both P_1 (N_0) centers and DBs. The EPR signals may be sensitive to ambient oxygen [4,14]. Panich *et al.* proposed that P_1 (N_0) centers are located within the diamond core whereas the DBs are mainly within the defect-rich interface layer [15,16]. Most of the ^{13}C nuclei in nanodiamonds are coupled with DB spins through hyperfine coupling. This coupling drastically shortens the ^{13}C nuclear spin lattice relaxation time [10,17]. These data highlight the fact that DBs seem to be located in the whole volume rather than close to the nanodiamond surface. N_0 PCs are reported to be mostly located in the disordered shells of nanodiamonds [14,18,19]. In these studies, the low amount of nitrogen-containing PCs compared to DBs is revealed by the absence of a triplet characteristic of ^{14}N nuclei. According to Fang *et al.*, the N_0 centers are located in the partially disordered shell [20]. This shell has a thickness of ∼1 nm and contains the DBs as well as the diamagnetic nitrogen defects, *i.e.* pairs of neighboring substitutional nitrogen atoms (N_2 or A center) or groups of four nitrogen around a vacancy (N_4 or B center) [20]. Such a location allows a weak hyperfine interaction to occur between the N_0 electron and hydrogen (fluorine) nuclear spins located at the nanodiamond surface [21]. In addition to atomic nitrogen centers N_0, nitrogen pairs N_2^+ and possibly vacancy centers with spin 3/2 (called R8 center) have been evidenced after sintering of DNDs [22,23]. H_1-center (the defect in diamond lattice containing one hydrogen atom, g-factor of 2.0028) is also reported in addition to the single line (g-factor of 2.0025) from other centers. A slight influence of ambient oxygen on the relaxation times T_1 and T_2 measured at the central field position allowed Fionov *et al.* [14] to propose that the single line spectrum can be due to the surface radicals, probably carbon-based DBs.

There are some discrepancies concerning the location of DB and P_1 (N_0) centers, either in the whole bulk or close to the surface, in the defect-rich interface layer. These differences may be explained by the different purification yields and the extend of the sp^2 carbon shell on the surface of the diamond core.

Another effect must be considered for DNDs: dipolar interaction of paramagnetic species with their interaction with paramagnetic O_2, which causes significant broadening of the EPR lines. The contribution of species located in the close vicinity of oxygen molecules decreases when the sample is transferred under low-O_2 atmosphere. This effect is reversible and has been evidenced by measurements in air and vacuum; an increase of 10 % of the signal intensity was observed without paramagnetic O_2 (under vacuum) [4]. Both P_1 (N_0)-centers and H_1-centers are reported as bulk defects and therefore do not interact with the ambient oxygen [14].

2.4 Investigation of the long-term stability of fluorinated DNDs

The fluorination of DND in our group, at the Institut de Chimie de Clermont-Ferrand (ICCF, Clermont-Ferrand, France), began almost ten years ago, which makes it possible to study the ageing for of the F-DND through a fluorinated sample during a previous study, subsequently named F-DNDold. The fluorination was performed in 2017 in static conditions in a two-step process. The temperature was increased to 450 °C and then stabilized for 12 h. After this first treatment and cooling to the ambient temperature, the reactor was flushed with nitrogen (N_2) flow for 1 h to remove unused F_2, HF and volatile fluorination products. To complete both sp^2-bonded C and H removal, the same sequence was repeated a second time (reference 11 of the main manuscript). This sample F-DNDold has recently been refluorinated in order to compare the impact of a second fluorination. This sample will be named F-F-DNDold. First of all, these samples were characterized by XRD to ensure that the diameter of the DNDs was preserved and that they were sufficiently crystalline (Figure S7). These diffractograms are compared with those of DND and the F-520-DND sample. No difference was observed between the three fluorinated samples, nor with the initial DND powder. The calculation of crystallite size shows a slight decrease in $< D >$ from 42 Å for DND to about 37.5-39 Å for the F-DND series, which represents a decrease in crystallite size of about 10%. The lattice parameter *a* is approximately 3.58-3.59 Å for the F-520-DND, compared to 3.57 Å for DND. The values of $< D >$ and *a* are summarized in Table S2.

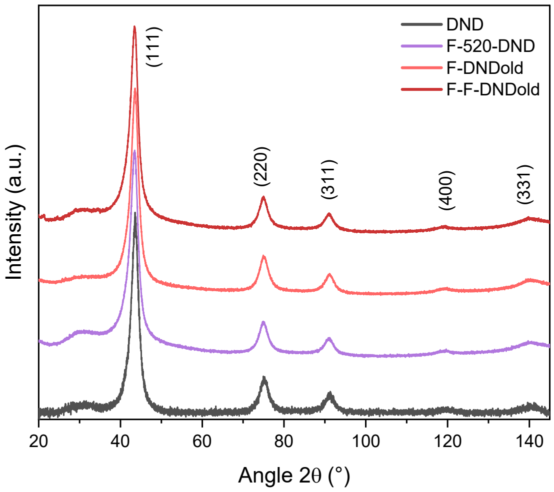

Figure S7 Diffractograms of the samples DND (black), F-520-DND (purple), an F-DND several years old (F-DNDold, orange) and its refluorinated version (F-F-DNDold, burgundy)

Table S2 Crystallite size < D > (in Å) and lattice parameter *a* (in Å) of the samples DND, F-520-DND, F-DNDold and F-F-DNDold.

	DND	F-520-DND	F-DNDold	F-F-DNDold
$< D >$ (Å)	41.9 ± 0.9	37.9 ± 0.9	39.2 ± 0.9	37.5 ± 0.9
a (Å)	3.572 ± 0.013	3.589 ± 0.015	3.583 ± 0.011	3.589 ± 0.014

The ageing and refluorination of F-520-DND does not alter the crystallinity of the DND or the size of the nanodiamond particles. FTIR was performed to probe possible chemical modifications of these fluorinated DNDs, particularly at their surface, which is the part most exposed to air. The FTIR spectra of F-DNDold and F-F-DNDold are compared to those of DND and F-DND (Figure S8). It can be seen that when fluorinated DNDs are exposed to air for 8 years, the OH band (3700-3000 cm^{-1}), $\nu_{C=O}$ (1730 cm^{-1}) and $\nu_{C=C}/\delta_{OH}$ (1640 cm^{-1}) vibration bands reappear. A slight change in the $C_{diamond}$ vibration at 1330 cm^{-1} is also visible for F-DNDold. Conversely, refluorination of F-DNDold (F-F-DNDold) eliminates all functional groups, restoring an FTIR spectrum identical to F-DND.

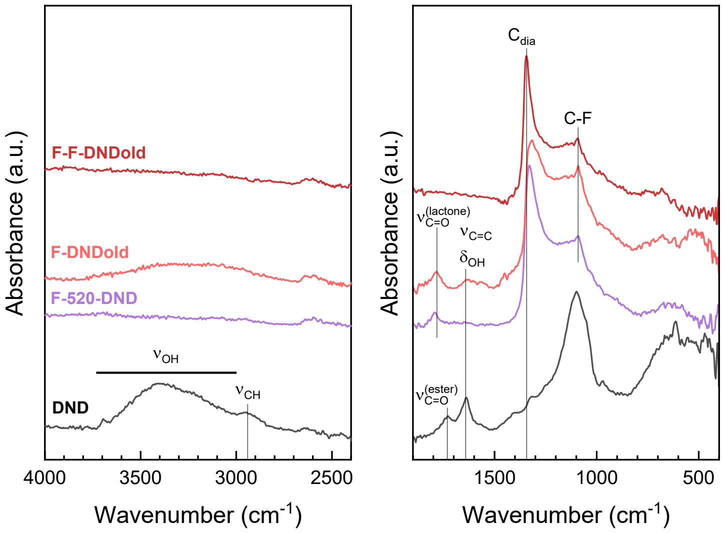

Figure S8 FTIR spectra of the samples DND (black), F-520-DND (purple), F-DNDold (orange) and F-F-DNDold (burgundy).

The ageing-induced modifications of the surface chemistry of fluorinated DNDs were investigated by NMR spectroscopy, focusing on the evolution of C–F bonds. The MAS NMR spectra of the ^{1}H, ^{13}C and ^{19}F nuclei were acquired for DND, F-520-DND, F-DNDold and F-F-DNDold (Figure S9). The ^{1}H spectrum (Figure S9a) indicates the presence of C-H bonds and/or C-OH groups for F-DNDold, while those of F-520-DND and F-F-DNDold do not contain any (not shown here). The ^{13}C spectrum (Figure S9b) of F-DNDold is similar to that of F-520-DND, although the broadening of the band caused by the C-C-F signal (42 ppm) appears less pronounced. In addition, the graphite band (120 ppm) is observed in the ^{13}C spectrum of F-DNDold. This shows that the sample has evolved over time and that graphitization has taken place. Conversely, the spectrum of F-F-DNDold no longer exhibits a $C_{graphite}$ signal, and the proportion of C–F bonds (84 ppm) is increased compared to F-520-ND, indicating conversion of graphite into $C_{ex\text{-}sp2}$-F bonds. To verify this hypothesis, the ^{19}F spectrum was studied (Figure S9c). The spectra of F-520-ND and F-DNDold were recorded at 14 kHz with a 4 mm rotor, as well as that of F-520-DND and F-F-DNDold recorded at 30 kHz with a 2.5 mm rotor. The spectrum of F-DNDold exhibit a shape identical to that of F-520-ND, with no visible decrease in the relative contents of the two types of C-F bonds, *i.e.* on the diamond surface and $C_{ex\text{-}sp2}$-F. The ^{19}F spectra of F-520-DND and F-F-DNDold are also identical, and no increase in the relative content of $C_{ex\text{-}sp2}$-F band (-180 ppm) is observed.

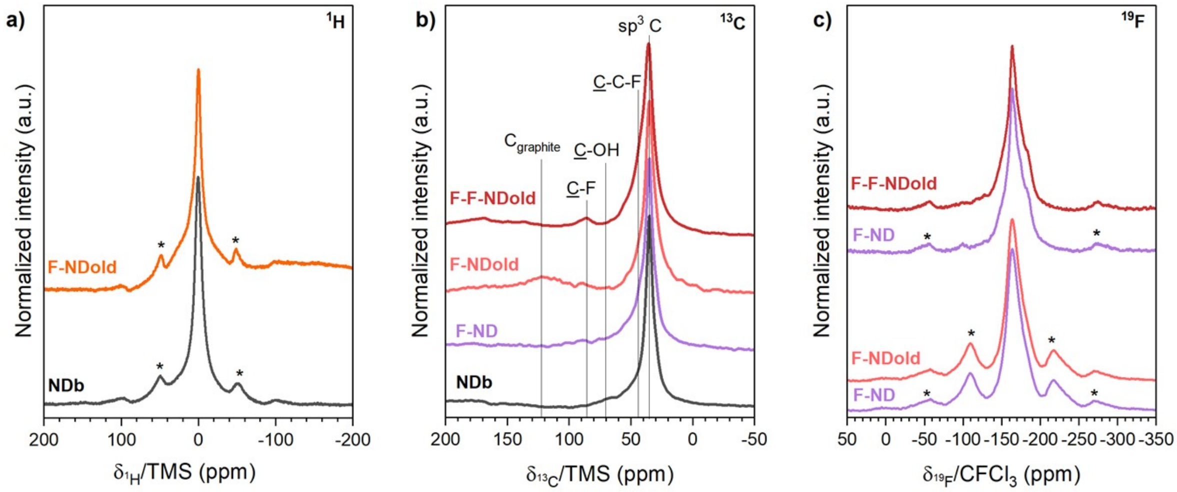

Figure S9 MAS-NMR spectra of the ^{1}H (a), ^{13}C (b) and ^{19}F (c) nuclei of the samples DND, F-520-DND, F-DNDold and F-F-NDold. The ^{1}H spectra of F-520-DND and F-F-NDold were not recorded because they do not have hydrogen atoms. The ^{19}F spectrum of F-520-DND and F-DNDold was recorded at 14 kHz (4 mm rotor), which explains the closer rotation bands.

2.5 Study of the influence of fluorination on metallic impurities of fluorinated DNDs

For the purpose of detecting, localizing and identifying the iron-based impurities in DNDs after their fluorination at 520 °C, imaging by HAADF-STEM and BF-STEM analysis was conducted on F-520-DND (Figures S10a and S10b). Both images illustrate an agglomerate of DND of several µm in size and a small particle (located at the bottom of the images) with higher electron density, appearing consequently brighter and darker in DF and BF images, respectively. Elemental X-mapping of carbon (K-edge), nitrogen (K-edge), fluorine (K-edge) and iron (K-edge) reveals that the observed agglomerate is mainly formed by carbon, with low amount of nitrogen (certainly coming from NV centers), fluorine is homogeneously distributed on the sample, probably grafted to the DND surface (Figures S10c-S10f). The small particle mainly contains fluorine and iron in agreement with its presence under the form of iron fluoride, FeF_3, found by Mössbauer.

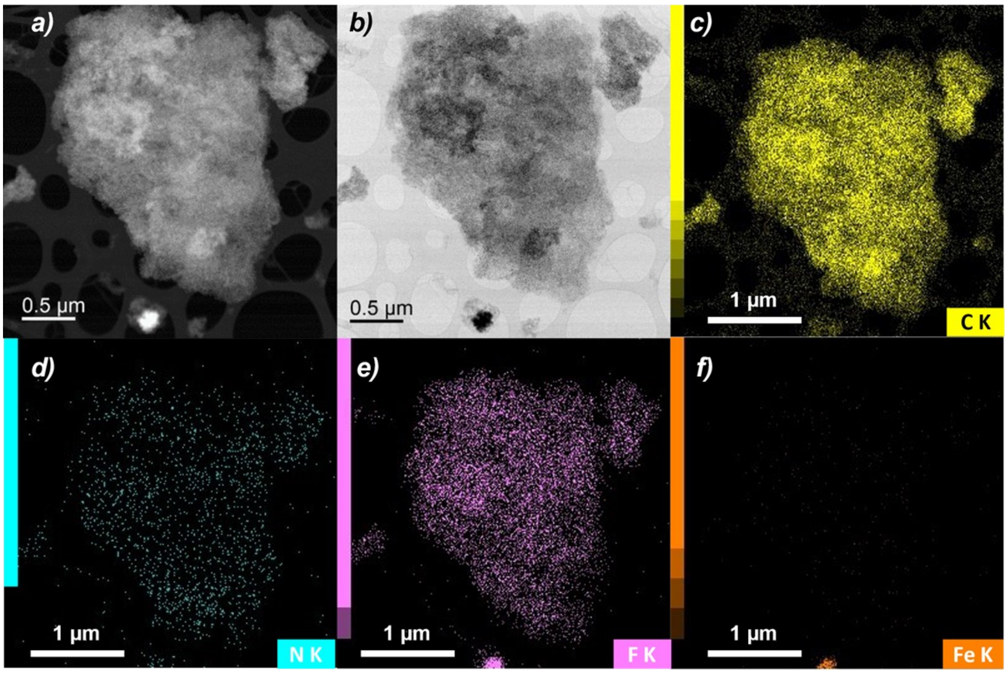

Figure S10 a) HAADF and **b)** BF-STEM images of a selected area of F-520-DND, respectively. **c-f)** corresponding EDX spectroscopy elemental mappings of carbon (K-edge) shown in yellow (**c**), nitrogen (K-edge) in light blue (**d**), fluorine (K-edge) in pink (**e**) and iron (K-edge) in orange (**f**).

A home-developed selective combustion method [24] was used to concentrate the inorganic impurities present in F-520-DND for their facile identification by FTIR (Figure S11). Compared with the impurities from the DND sample (O-DND), those coming from F-520-DND (O-F-520-DND), show a radically different IR spectrum. Indeed, the Si-O-Si vibrational bands are no longer visible after fluorination of DND. This clearly reflects the effective removal of SiO_2 by fluorination, in agreement with detection of released Si_xF_y species during room-temperature fluorination of DND powder. Four broad bands appear in the FTIR spectrum of O-F-520-DND at 455, 575, 870 and 1030 cm^{-1}. The two first bands could be either assigned to non-fluorinated Cr_2O_3 vibrations at 413 (E_u^1), 445 (E_u^2), 540 (A_{2u}^1 and E_u^3) and 612 cm^{-1} (A_{2u}^2 and E_u^4) and/or to Fe-F bonds belonging to FeF_2 and FeF_3 compounds expected in the range 450-735 cm^{-1}, respectively [25–29].

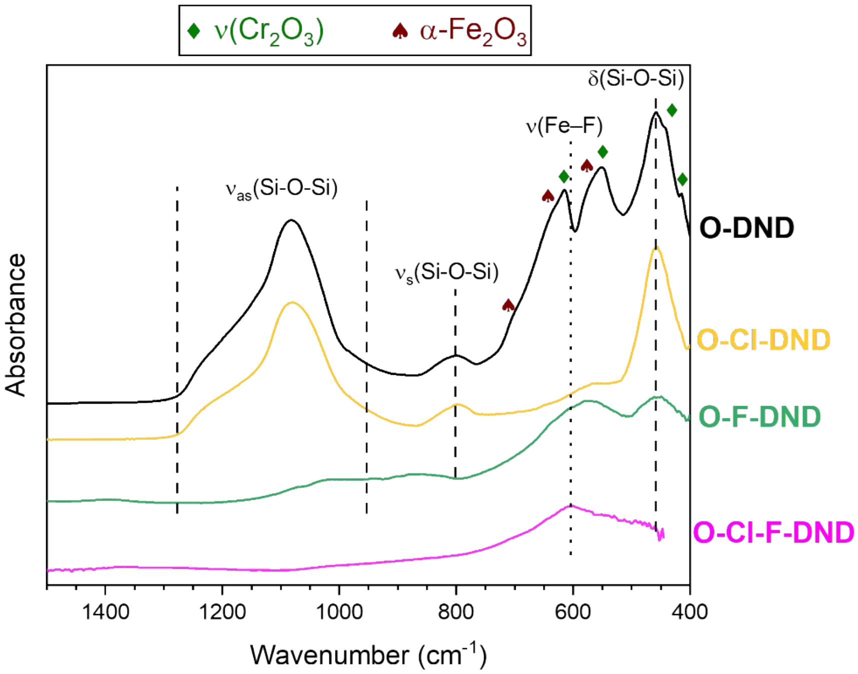

Figure S11 FTIR spectrum of resulting ashes after selective combustion in air of raw DND (O-DND), Cl-650-DND (O-Cl-650-DND), F-520-DND (O-F-520-DND) and Cl-F-DND (O-Cl-F-DND).

2.6 Nanodiamond core *vs.* nanodiamond surface modification

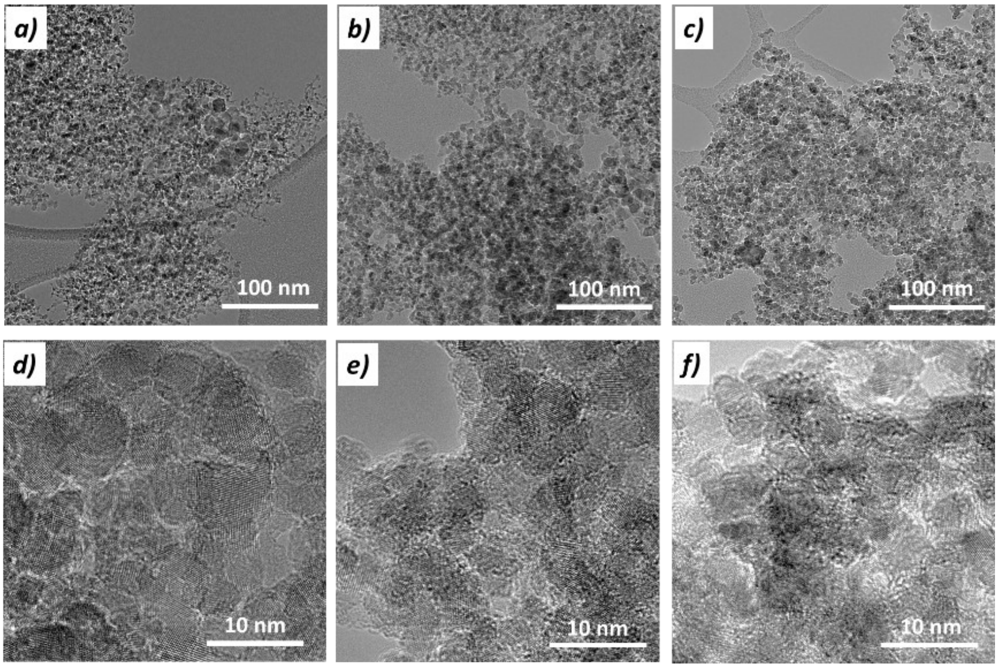

Figure S12 TEM micrograph of a) and d) the used raw DNDs, b) and e) the DNDs after chlorination (at 650 °C for 1 h flowrate of 20 mL/min, Cl-650-DND, and, c) and f) the DNDs after chlorination followed by fluorination (F-Cl-DND).

Dispersion tests of DNDs were carried out in ethanol and in water to evaluate the effect of surface functionalization on colloidal stability. Raw DNDs, bearing oxygenated surface groups, disperse readily in water. In ethanol, reduced dissociation of surface groups leads to weaker electrostatic repulsion and consequently poorer dispersion stability, with a greater tendency toward aggregation. In contrast, chlorinated DNDs and fluorinated DNDs, Cl-650-DND, F-520-DND and F-Cl-DND, are dispersed in ethanol, demonstrating that halogenation significantly improves dispersibility in ethanol, as already reported.[30] In water, a different behavior was observed. Chlorinated DNDs tend to remain in dispersion even if their faster sedimentation than that observed in ethanol is noticeable by a transparent sedimentation front below the liquid-air meniscus. Fluorinated DNDs (both F-520-DND and F-Cl-DND, even if the effect is less pronounced for this latter) showed a far less poorer dispersion ability in water than it is observed in ethanol. Presence of fluorine groups reduces the affinity of DND surfaces for water, likely due to increased hydrophobic character.

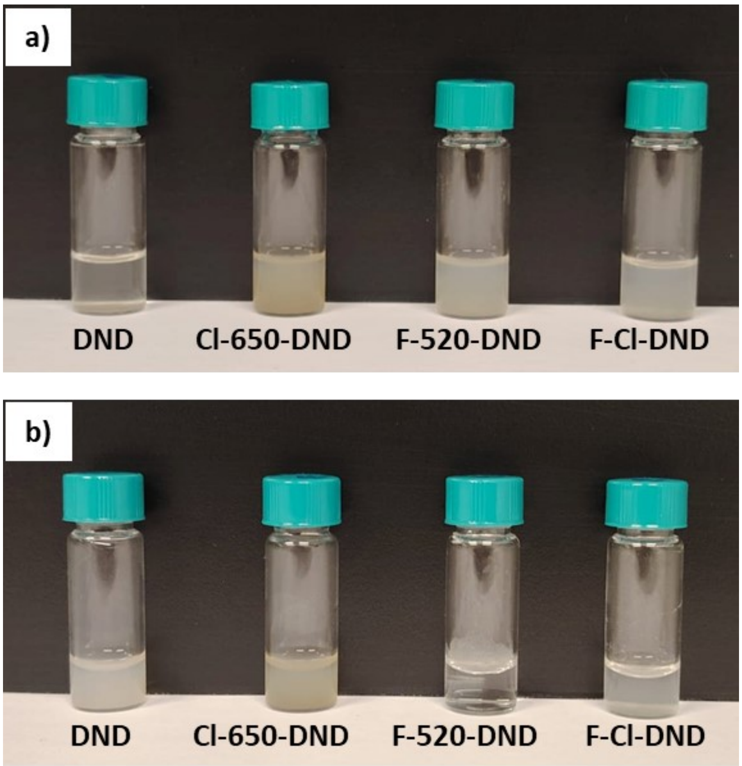

Figure S13 Pristine (DND), chlorinated (Cl-650-DND), fluorinated (F-520-DND) and DND treated by chlorination followed by fluorination (F-Cl-DND) dispersions a) in ethanol and b) in water and settled for 5 h.

2.7 Surface modification of F-Cl-DND

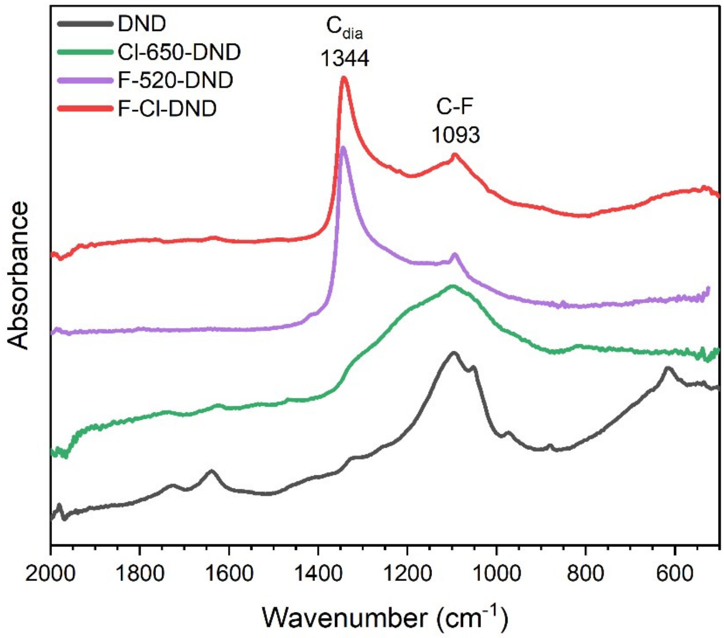

Figure S14 FTIR spectrum DND (raw DNDs), Cl-650-DND (DNDs chlorinated at 650 °C for 1 h with a Cl_2 flowrate of 20 mL/min), F-520-DND (DNDs fluorinated for 12 h at 520 °C) and F-Cl-DND (DNDs chlorinated at 650 °C for 1 h flowrate of 20 mL/min and fluorinated for 12 h at 520 °C).

3 References

1 G. Herzberg, *Molecular Spectra Vol I*, D.Van Nostrand Company Inc., 1950.

2 S. V. Khristenko, V. P. Shevelko and A. I. Maslov, in *Molecules and Their Spectroscopic Properties*, eds. S. V. Khristenko, V. P. Shevelko and A. I. Maslov, Springer, Berlin, Heidelberg, 1998, pp. 87–121.

3 H. Lefebvre-Brion and R. W. Field, *The spectra and dynamics of diatomic molecules*, Elsevier, Amsterdam, Revised and enlarged edition., 2004.

4 A. I. Shames, A. M. Panich, L. Friedlander and V. Yu. Dolmatov, *Diam. Relat. Mater.*, 2023, **136**, 110059.

5 A. M. Panich, A. I. Shames, D. Mogilyansky, S. D. Goren and V. Yu. Dolmatov, *Diam. Relat. Mater.*, 2020, **108**, 107918.

6 A. I. Shames, A. M. Panich, W. Kempiński, A. E. Alexenskii, M. V. Baidakova, A. T. Dideikin, V. Yu. Osipov, V. I. Siklitski, E. Osawa, M. Ozawa and A. Ya. Vul', *J. Phys. Chem. Solids*, 2002, **63**, 1993–2001.

7 O. E. Andersson, B. L. V. Prasad, H. Sato, T. Enoki, Y. Hishiyama, Y. Kaburagi, M. Yoshikawa and S. Bandow, *Phys. Rev. B*, 1998, **58**, 16387–16395.

8 B. L. V. Prasad, H. Sato, T. Enoki, Y. Hishiyama, Y. Kaburagi, A. M. Rao, P. C. Eklund, K. Oshida and M. Endo, *Phys. Rev. B*, 2000, **62**, 11209–11218.

9 K. Iakoubovskii, M. V. Baidakova, B. H. Wouters, A. Stesmans, G. J. Adriaenssens, A. Ya. Vul' and P. J. Grobet, *Diam. Relat. Mater.*, 2000, **9**, 861–865.

10 M. Dubois, K. Guérin, E. Petit, N. Batisse, A. Hamwi, N. Komatsu, J. Giraudet, P. Pirotte and F. Masin, *J. Phys. Chem. C*, 2009, **113**, 10371–10378.

11 M. Dubois, K. Guérin, N. Batisse, E. Petit, A. Hamwi, N. Komatsu, H. Kharbache, P. Pirotte and F. Masin, *Solid State Nucl. Magn. Reson.*, 2011, **40**, 144–154.

12 L. B. Casabianca, A. I. Shames, A. M. Panich, O. Shenderova and L. Frydman, *J. Phys. Chem. C*, 2011, **115**, 19041–19048.

13 V. Kuzmin, K. Safiullin, G. Dolgorukov, A. Stanislavovas, E. Alakshin, T. Safin, B. Yavkin, S. Orlinskii, A. Kiiamov, M. Presnyakov, A. Klochkov and M. Tagirov, *Phys. Chem. Chem. Phys.*, 2018, **20**, 1476–1484.

14 A. V. Fionov, A. Lund, W. M. Chen, N. N. Rozhkova, I. A. Buyanova, G. I. Emel'yanova, L. E. Gorlenko, E. V. Golubina, E. S. Lokteva, E. Ōsawa and V. V. Lunin, *Chem. Phys. Lett.*, 2010, **493**, 319–322.

15 A. M. Panich, N. A. Sergeev and S. D. Goren, *Solid State Nucl. Magn. Reson.*, 2020, **105**, 101624.

16 A. M. Panich, H.-M. Vieth, A. I. Shames, N. Froumin, E. Ôsawa and A. Yao, *J. Phys. Chem. C*, 2010, **114**, 774–782.

17 D. Yoon, M. Soundararajan, S. Sekatski, J. Genoud, S. Alberti and J.-P. Ansermet, *J. Phys. Chem. C*, 2019, **123**, 21237–21243.

18 C. Presti, A. S. L. Thankamony, J. G. Alauzun, P. H. Mutin, D. Carnevale, C. Lion, H. Vezin, D. Laurencin and O. Lafon, *J. Phys. Chem. C*, 2015, **119**, 12408–12422.

19 P. G. Baranov, I. V. Il'in, A. A. Soltamova, A. Ya. Vul', S. V. Kidalov, F. M. Shakhov, G. V. Mamin, S. B. Orlinskii and M. Kh. Salakhov, *JETP Lett.*, 2009, **89**, 409–413.

20 X. Fang, J. Mao, E. M. Levin and K. Schmidt-Rohr, *J. Am. Chem. Soc.*, 2009, **131**, 1426–1435.

21 B. V. Yavkin, D. G. Zverev, G. V. Mamin, M. R. Gafurov and S. B. Orlinskii, *J. Phys. Chem. C*, 2019, **123**, 22384–22389.

22 A. A. Soltamova, I. V. Ilyin, P. G. Baranov, A. Ya. Vul', S. V. Kidalov, F. M. Shakhov, G. V. Mamin, S. B. Orlinskii, N. I. Silkin and M. Kh. Salakhov, *Phys. B Condens. Matter*, 2009, **404**, 4518–4521.
23 C. a. J. Ammerlaan, *Impurities Defects Group IV Elem. III-V Compd.*
24 K. Henry, M. Emo, S. Diliberto, S. Hupont, J.-C. Arnault, H. Girard, M. Dubois and B. Vigolo, *Diam. Relat. Mater.*, 2023, **140**, 110466.
25 I. Plitz, F. Badway, J. Al-Sharab, A. DuPasquier, F. Cosandey and G. G. Amatucci, *J. Electrochem. Soc.*, 2004, **152**, A307.
26 M. Balkanski, P. Moch and G. Parisot, *J. Chem. Phys.*, 1966, **44**, 940–944.
27 J. Giordano and C. Benoit, *J. Phys. C Solid State Phys.*, 1988, **21**, 2749.
28 S. B. Osin, D. I. Davliasthin and J. S. Ogden, *J. Fluor. Chem.*, 1996, **76**, 187–192.
29 S. Bouketaya, M. Smida, M. S. M. Abdelbaky, M. Dammak and S. García-Granda, *J. Solid State Chem.*, 2018, **262**, 343–350.
30 H. Huang, Y. H. Wang, J. B. Zang and L. Y. Bian, *Appl. Surf. Sci.*, 2012, **258**, 4079–4084.